Article

K/Ka-Band Very High Data-Rate Receivers: A Viable Solution for Future Moon Exploration Missions

Federico Alimenti [1,*], Paolo Mezzanotte [1], Luca Roselli [1], Valentina Palazzi [1],
Stefania Bonafoni [1], Roberto Vincenti Gatti [1], Luca Rugini [1,2], Giuseppe Baruffa [1],
Fabrizio Frescura [1,2], Paolo Banelli [1,2], Federico Bernardi [3], Fabrizio Gemma [3],
Gianni Nannetti [4], Paolo Gervasoni [5], Paolo Glionna [5], Enrico Pagana [6], Giambattista Gotti [7],
Paolo Petrini [8], Francesc Coromina [9], Federico Pergolesi [10], Mario Fragiacomo [10],
Alessandro Cuttin [10], Erica De Fazio [10], Federico Dogo [10] and Anna Gregorio [10,11]

1   Department of Engineering, University of Perugia, via G. Duranti 93, 06125 Perugia, Italy;
    paolo.mezzanotte@unipg.it (P.M.); luca.roselli@unipg.it (L.R.); palazzi.valentina.89@gmail.com (V.P.);
    stefania.bonafoni@unipg.it (S.B.); roberto.vincentigatti@unipg.it (R.V.G.); luca.rugini@unipg.it (L.R.);
    giuseppe.baruffa@unipg.it (G.B.); fabrizio.frescura@unipg.it (F.F.); paolo.banelli@unipg.it (P.B.)
2   Consorzio Nazionale Interuniversitario per le Telecomunicazioni (CNIT), 43124 Parma, Italy
3   GMSpazio s.r.l., Viale Guglielmo Marconi, 19, 00146 Rome, Italy; federico.bernardi@gmspazio.com (F.B.);
    fabrizio.gemma@gmspazio.com (F.G.)
4   Silicon Infusion, CP House, Otterspool Way, Watford WD25 8HP, UK; gianni_nannetti@siliconinfusion.com
5   Analog Devices, Energy Park, 20871 Vimercate (MB), Italy; Paolo.Gervasoni@analog.com (P.G.);
    Paolo.Glionna@analog.com (P.G.)
6   Independent Researcher, 1023 Chieri (TO), Italy; enrico.pagana@gmail.com
7   Independent Researcher, 24030 Valbrembo (BG), Italy; herrgots@gmail.com
8   Department of Electronics and Telecommunications, Politecnico di Torino, 10129 Torino, Italy;
    paolo.petrini@polito.it
9   ESA-ESTEC, Keplerlaan 1, 2201 AZ Noordwijk, The Netherlands; Francesc.Coromina@esa.int
10 PicoSaTs s.r.l., Padriciano 99, c/o Area Science Park, 34149 Trieste, Italy; federicopergolesi@picosats.eu (F.P.);
    mario@picosats.eu (M.F.); alessandro@picosats.eu (A.C.); ericadefazio@picosats.eu (E.D.F.);
    federicodogo@picosats.eu (F.D.); anna.gregorio@ts.infn.it (A.G.)
11 Department of Physics, University of Trieste, via Valerio 2, 34149 Trieste, Italy
*   Correspondence: federico.alimenti@unipg.it; Tel.: +39-075-585-3642; Fax: +39-075-585-3654

Abstract: This paper presents a feasibility study for a very high data rate receiver operating in the K/Ka-band suitable to future Moon exploration missions. The receiver specifications are outlined starting from the mission scenario and from a careful system analysis. The designed architecture uses a low noise front-end to down-convert the incoming K/Ka-band signal into a 3.7 GHz intermediate frequency (IF). For maximum flexibility, a software defined radio (SDR) is adopted for the I/Q demodulation and for the analog to digital conversion (ADC). The decoding operations and the data interface are carried out by a processor based on field programmable gate array (FPGA) circuits. To experimentally verify the above concepts, a preliminary front-end breadboard is implemented, operating between 27.5 and 30 GHz. The breadboard, which uses components off the shelf (COTS) and evaluation boards (EVBs), is characterized by a 46 dB gain, a 3.4 dB noise figure and a −37 dBm input-referred 1 dB compression point. Finally, a 40 Msym/s quadrature phase shift keying (QPSK) signal is demodulated by means of a commercially available SDR, demonstrating the above concept. The importance of these results is that they have been obtained exploiting a class of miniaturized and low cost microwave integrated circuits currently available on the market, opening the way to a dense communication infrastructure on cislunar space.

1. Introduction

The current trend in space exploration is the planning of more missions to study Earth's nearest celestial bodies. To enable human expansion across the solar system, an outpost for crewed missions to the Moon, that also supports scientific discovery, and a concept of human controlled robotic lunar exploration are key passages: Moreso, they are prerequisite instances to allow a permanent presence of manned missions outside the planet Earth. Hence, cislunar space is becoming the target for a variety of projects, such as the Lunar Orbital Platform-Gateway (LOP-G) and Lunar Relay Satellites (LRS). This explains why there is a significant effort for the development of new technologies that will allow the establishment of Moon bases or stations; in this framework an appropriate telecommunications infrastructure is demanded as well. Such infrastructure should have the capability of carrying out the simultaneous multi band communications between the Earth, the Moon, including visiting (rovers) and descent/ascent (landers, terminals) vehicles, and other elements in cislunar orbit (LOP-G, LRS). Since this kind of mission employs many information intensive (i.e., high resolution, high coverage, high duty cycle) sensors demanding high speed link capabilities, data volume requirements are expected to increase [1]. Moreover, when considering human exploration, a high data rate is compulsory [2,3].

In this context the high portion of the microwave frequency band emerges from the others, mainly for three reasons: First, largest bandwidths can be exploited; second, the expected received energy is higher for the same link conditions and ground stations; and third, high performance integrated circuits (IC) operating at these frequencies are available form the cellular and base station market. Concerning the first motivation, it is evident that the 1500 MHz bandwidth allocated in the 26 GHz K-band is four times larger than the 375 MHz bandwidth allocated in the 8025–8400 MHz X-band. Assuming the same spectral efficiency in information bit/s per Hz (which is the case for a given coding, modulation and filtering scheme) the availability of an expanded spectrum results in a linear increase in the data rate and, potentially, in the data volume that can be transmitted. In other words, the K-band should allow users to transmit about four times more data than the X-band. Even the International Telecommunication Union (ITU) and the Space Frequency Coordination Group (SFCG) recommend the K-band for high data rate communications in the lunar region [4].

With respect to the second motivation, it is worth observing that, all else being equal (antenna aperture), the performance increase in the link budget is proportional to the square of the ratio of the new frequency to the former one. This increase occurs because the narrower beam concentrates more energy on the receiver. However, other factors create challenges when high frequencies are used.

K-bands are the portions of the electromagnetic spectrum, in the microwave range of radio frequencies (RF), ranging between 18 and 26.5 GHz (K-band) and between 27 and 40 GHz (Ka-band). Being necessary to support human exploration, uplink frequency allocation between 22.55–23.15 GHz (K-band) and between 27.5–30 GHz (Ka-band) are of special interest as their use in cislunar applications is novel, which means that there is a need to implement space receiver technology in this band for space research (SR) applications.

A main challenge affecting the use of these high frequency bands is the high Doppler frequency shift, that is directly proportional to the relative transmitter-receiver velocity, and inversely to the wavelength. This issue is not considered critical, but does need to be taken into account.

In this paper, a comprehensive analysis is carried out to highlight the need for a receiver on K-bands that supports high speed links in cislunar exploration scenarios. The main features of the receiver are: (i) to enable communication from Earth to lunar orbit (E-LO), from Earth to lunar surface (E-LS) and from a lunar orbit to lunar surface (LO-LS), even in low signal-to-noise ratio (SNR)

conditions; (ii) to acquire, demodulate and decode, with a low-density parity-check (LDPC) approach, uplink signals in the 22.55–23.15 GHz or in the 27.5–30 GHz bands, covering different data rates up to 100 Mbps; (iii) to implement the modulation schemes required by the Consultative Committee for Space Data Systems (CCSDS) and to the European Cooperation for Space Standardization (ECSS), both in the classical way (based on ground-aided acquisition approach) and in autonomous mode (non-ground-aided). Another important requirement is to keep the power consumption below 12 W in such a way as to be compatible with the solar panels available on the market [5,6].

The original contribution of the present paper is twofold. First of all we propose a Ka-band receiver suitable for deep space mission that is based on off-the-shelf components developed for commercial telecommunication systems. This is a quite novel approach that, once demonstrated, could dramatically reduce mission costs and open the way to the massive adoption of cubesats even in the Moon exploration context [7]. The Mars Cube One (MarCO) satellites, for example, are two notable precursors of such a vision [8]. Another original contribution of this work is related to the methodology used to model the phase-noise impairments. In low-cost radios the local oscillator signal is generated by an integrated frequency synthesizer, the phase-noise of which is typically worse than that obtained with expensive dielectric resonator oscillators (DRO). As a consequence the phase-noise impairments need to be carefully considered in the link budget. The state of the art for simultaneous orbit and link budget computations is Systems Tool Kit (STK), a multi-physics software from Analytical Graphics, Inc. [9]. This software, however, is unable to simulate the oscillator phase-noise. To solve such problem it is shown that, in the small phase errors approximation, the phase noise can be modeled as an equivalent thermal noise. This approach leads to the definition of an effective noise figure (accounting for both the thermal and the phase-noise): A simple formula that can be easily implemented in the STK to allow a preliminary study of the phase-noise impairments.

2. Basic Link Budget

Before presenting a detailed analysis, some basic considerations are introduced here in order to estimate the receiver signal levels. Figure 1 shows a simplified link geometry where the receiver is on the Moon (M) surface, exactly at the zenith of a ground station on the Earth (E). In this figure G_a^{TX} and G_a^{RX} are the gains of the ground station and of the satellite antennas respectively, P_{TX} is the transmitted power and R is the average Earth-to-Moon distance.
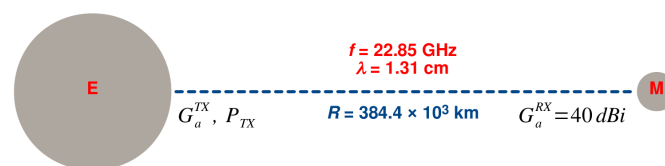
Figure 1. Link geometry. To estimate the maximum signal level the receiver is assumed on the Moon (M) surface, perfectly at the ground station Zenith on Earth (E). Link parameters: $R = 384.4 \times 10^3$ km, transmitted power $P_{TX} = 100$ W, transmitting antenna gain $G_a^{TX} = 65$ dBi (10 m dish antenna with a 60% efficiency), receiving antenna gain $G_a^{RX} \approx 40$ dBi.

The received power P_{RX} can be determined applying the Friis' formula to such a link geometry:

$$P_{RX} = G_a^{TX} G_a^{RX} \left(\frac{\lambda}{4\,\pi\,R} \right)^2 P_{TX} \tag{1}$$

where λ is the carrier wavelength. In this relationship, the atmospheric attenuation is not considered because the scope of the basic analysis is the determination of the maximum received signal level. Table 1 reports an evaluation of the path losses in both the K and Ka frequency bands for $R = 384.4 \times 10^3$ km. Note that going from the K to the Ka band leads to a 2 dB increase of the path loss

(i.e., from about 231 to about 233 dB), but that such an increase is exactly counteracted by a greater gain of the fixed-diameter receiving antenna.

Although reflectarrays [10], reconfigurable phased arrays [11] or flat-plate antenna solutions with efficiency as high as 85% [12] could be employed, a 50 cm dish antenna is considered here for simplicity. Such a size is compatible with the deployable parabolic reflectors recently developed by several authors [7,8] for cubesat applications. The antenna gain G_a and the half power beam width Θ_h can be estimated, for a given diameter D and efficiency η_a, with the following relationships:

$$G_a = \eta_a \left(\frac{\pi D}{\lambda} \right)^2 \tag{2}$$

$$\Theta_h = \frac{2\lambda}{\sqrt{\pi D}} \tag{3}$$

A receiving antenna with $D_{RX} = 50$ cm has gain of about 39 dBi in K-band and reaches 41 dBi in the Ka-band, as reported in Table 1.

Table 1. Earth-Moon Free-Space Losses in the K/Ka-Bands and Receiver Antenna Gains.

Band	f_0 (GHz)	λ (cm)	R (km)	Path Loss (dB)	D_{RX} (cm)	η_a^{RX} (%)	G_a^{RX} (dBi)	Θ_h^{RX}
K	22.85	1.31	384.4×10^3	231.3	50	60	39.4	$1.7°$
Ka	28.65	1.05	384.4×10^3	233.3	50	60	41.3	$1.4°$

As a first assumption, the antenna diameter at the ground station is $D_{TX} = 10$ m (transmitting antenna, uplink). Considering an antenna efficiency $\eta_a^{TX} = 60\%$, a 65 dBi gain and a 5.1 arcmin half-power beam width are obtained, the latter value being about $1/6$ of the the angular diameter of the Moon seen from the Earth. A reasonable value for the transmitted power is $P_{TX} = 100$ W, that corresponds to $+50$ dBm. As a consequence the effective isotropic radiated power (EIRP) at the ground station is:

$$EIRP_{TX} = G_a^{TX} P_{TX} \approx 65.4 + 50 = 115.4 \text{ dBm} \tag{4}$$

where this quantity is evaluated at 22.85 GHz, i.e., in the K-band. Other EIRP values are quoted in Table 2 for different antenna diameters and different frequencies.

Table 2. Transmitter EIRP and Received Power in the K/Ka-Bands versus D_{TX}.

Band	f_0 (GHz)	λ (cm)	P_{TX} (W)	D_{TX} (m)	η_a^{TX} (%)	G_a^{TX} (dBi)	Θ_h^{TX} (arcmin)	$EIRP_{TX}$ (dBm)	Path Loss (dB)	G_a^{RX} (dBi)	P_{RX} (dBm)
K	22.85	1.31	100	10	60	65.4	5.1	115.4	231.3	39.4	-76.5
				3	60	54.9	16.9	104.9			-87.0
Ka	28.65	1.05	100	10	60	67.3	4.1	117.3	233.3	41.3	-74.7
				3	60	56.8	13.6	106.8			-85.2

The same table also quotes the power levels received on the Moon. These levels are the absolute maximum and should be significantly above the receiver noise floor in order to guarantee for non zenithal links and atmospheric attenuation. As an example, a rain rate of 10 mm/h at 23 GHz results in a specific atmospheric loss of 2 dB/km. Integrating over a typical rain path of 5 km, an atmospheric attenuation of 10 dB is estimated, according to International Telecommunication Union, ITU-R P.838-2 [13].

Noise Floor and Noise Margins

The noise floor N_i represents the equivalent noise power referred at the receiver input. It is a function of the system noise temperature T_{sys} and of the minimum intermediate frequency (IF) bandwidth B_{IF} (i.e., of the signal bandwidth) according to:

$$N_i = k_B \, T_{sys} \, B_{IF} \tag{5}$$

where $k_B = 1.38 \times 10^{-23}$ J/K is the Boltzmann constant. The system noise temperature, in turn, is related to the antenna noise temperature T_a and to the receiver noise figure F_{RX} by:

$$T_{sys} = T_a + (F_{RX} - 1) \, T_0 \tag{6}$$

$T_0 = 290$ K being the standard IEEE temperature for noise. It has already been pointed out that, with a 50 cm parabolic dish as the receiver antenna, a half power beam width of $1.7°$ is obtained (see Table 1). This value is smaller than the $1.9°$ angular diameter of the Earth seen by the Moon (The angular diameter of the Earth seen by the Moon is $\delta_{e,m} \approx 1.9°$, that of the Moon seen by the Earth, instead, is $\delta_{m,e} \approx 0.5°$). As a consequence the main beam of the receiver antenna is completely filled by the Earth and the corresponding antenna noise temperature is close to the brightness temperature of the Earth surface. A conservative estimation thus gives $T_a \approx T_0 = 290$ K.

Performing the computations in (6) for a receiver noise figure $F_{RX} = 3$ dB, a system noise temperature $T_{sys} = 580$ K is obtained. For a maximum IF bandwidth of 50 MHz (i.e., at the maximum data rate), a receiver noise floor $N_i = -94$ dBm is estimated. Reducing the IF bandwidth (and thus the data rate) to 5 MHz and 500 kHz, the noise floor decreases to -104 and -114 dBm respectively. The latter estimations, however, hold only when the phase noise of the local oscillators (LO) contained in the receiver is negligible (see Section 4.2).

Concluding this basic analysis one can observe that, in the K-band, the nominal $+115.4$ dBm EIRP at the ground station, is able to establish a -76.5 dBm power at the receiver input, and that this value is about 17.5 dB above the noise floor for a 50 MHz signal bandwidth. As already stated, however, such a margin represents a best case situation; lower values have to be expected in the presence of non zenithal links and atmospheric attenuation.

3. Mission Scenario

Future Moon explorations will be characterized by quite complex mission scenarios, as many different vehicles and spacecrafts will be involved [2]. Preliminary plans from the major space agencies foresee the usage of a LOP-G in cislunar orbit, the adoption of a small- to medium-size constellation of space vehicles or LRS around the Moon, and lunar surface elements (LSEs) such as rovers, landers and so on. All these vehicles should be able to communicate with each other and with the ground stations on the Earth. Finally, for the LRS, cubesats could be adopted, which calls for further constraints due to the well-known limitations of these platforms with respect to size, mass and power consumption.

After the basic considerations of the previous section, a more in-depth mission scenario is considered here. All the simulations were performed with STK, [9]. In creating the scenario, only the case of a direct communication between Earth and Moon was considered (i.e., no repeaters and no transponders), since this is the most critical situation (greater link distance, presence of the Earth atmosphere). Three ground stations were assumed on the Earth (with the transmitters), namely:

- ESRIN (Lat. $41.83°$ N, Lon. $12.68°$ E),
- New Norcia (Lat. $31.04°$ S, Lon. $116.19°$ E),
- Guiana Space Center (Lat. $5.23°$ N, Lon. $52.77°$ W),

The receiver, instead, was on a base located near the South pole of the Moon (Lat. $66.41°$ S, Lon. $9.82°$ W). The disposition of these ground stations guarantees a full coverage of the Moon.

The receiver, on the other hand, has been positioned on the face of the Moon visible from the Earth. For realistic simulations, the Earth atmosphere model was included. The analysis considered also the motion of the celestial bodies and their influence on the communication.

Each ground station is equipped with a 10 m parabolic antenna and, according to Table 2, transmits a power of 100 W in the K-band at 22.85 GHz. A data stream of 100 Mbit/s modulates the carrier with a quadrature phase shift keying (QPSK) constellation, so that the resulting signal bandwidth is of about 50 MHz. To improve the environment simulation, some models were included in the scenario, like: (i) the ITU-R P.618, to model the total propagation losses; (ii) the ITU-R P.676-9, to model the atmospheric absorption due to gases [14].

Regarding the receiver, likewise the transmitters, a parabolic antenna with the same efficiency is assumed but, in this case, with a 50 cm diameter (see Table 1). The receiver noise figure is $F_{RX} = 3$ dB and the corresponding system noise temperature is modeled according to (6). Finally, STK computes the antenna noise temperature using Sun, atmospheric and cosmic background noise models. Depending on the modulation scheme used in the transmission, the demodulator can be selected automatically by the software and is useful for bit error rate (BER) estimations.

The computations were performed on a time interval of one month, from the first of January 2025 to the first of February of the same year. As it is understandable, depending on the ground station position and calculation time, the results may vary significantly. Thus, two case studies are considered onwards. The first one is when only two ground stations are visible from the Moon, namely: ESRIN and New Norcia. In the second case, instead, all three ground stations are in visibility to the Moon base. Figure 2 reports Moon-centered and Earth-centered visuals in two different days: 1 January 2025 (first case of study) and 17 January 2025 (second case of study).

(**a**) 1st January 2025
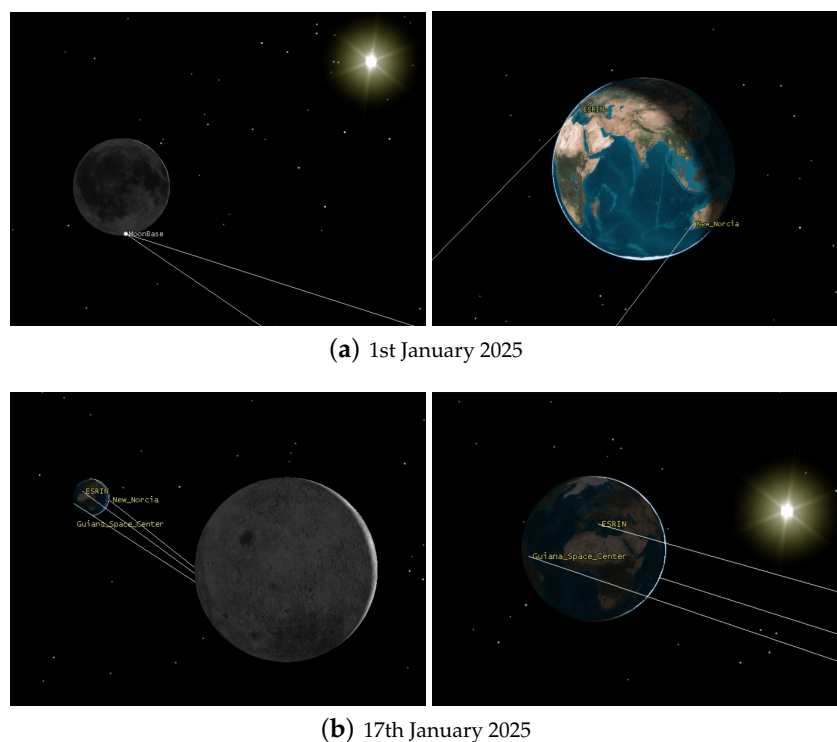
(**b**) 17th January 2025

Figure 2. Distances and angles. Moon centered and Earth centered visuals in two different days; (**a**) 1 January 2025 and (**b**) 17 January 2025. In the first case, two ground stations (ESRIN and New Norcia) are visible from the Moon; in the second case, the visibility is extended to three ground stations (ESRIN, New Norcia and Guiana Space Center). The simulations have been carried out with STK.

The main results are quoted in Table 3 for the two different situations. Here C/N is the carrier-to-noise ratio and E_b/N_0 is the energy per bit to noise power spectral density ratio ($\frac{E_b}{N_0} = \frac{C}{N} \frac{B}{f_b}$

where B is the signal bandwidth and f_b is the data rate). In all the cases STK assumes that the receiver antenna is pointed to each of the visible ground stations. As a consequence the best achievable link characteristics can be studied in the different situations. Note that the antenna noise temperature changes as a function of the pointing directions; this because the fraction of the main antenna beam covered by the Earth also changes. Another interesting fact is that, in the second case, the Guiana Space Center station, although visible from the Moon, is affected by very high atmospheric losses. This is because the signal path is nearly tangent to the Earth surface, experimenting a longer atmospheric propagation and terrain scattering.

Table 3. Results of the Mission Scenario Simulations carried out with Systems Tool Kit (STK).

| Time (UTC)	Ground Stations	Path Loss (dB)	Atm. Loss (dB)	Doppler (kHz)	T_a (K)	C/N (dB)	E_b/N_0 (dB)
1 January 2025; 10:00	ESRIN	231.2	1.2	+17.65	57.7	18.5	15.5
	New Norcia	231.1	1.7	−21.43	75.1	17.9	14.9
	Guiana S.C.			out of visibility			
17 January 2025; 00:00	ESRIN	231.4	0.4	+7.65	21.8	19.6	16.6
	New Norcia	231.5	11.4	−31.36	223.5	6.3	3.3
	Guiana S.C.	231.5	81.7	+29.77	242.7	−64.2	−67.2

10 m dish antenna with 100 W TX power at 22.85 GHz; QPSK modulation with 50 MHz signal bandwidth.

In conclusion, the detailed simulation of the mission scenario shows the possibility of a stable communication using a minimum of three transmitters on Earth. For a more continuous communication, however, it is recommended to increase the ground stations number to contrast the effects due to the motion of celestial bodies and atmosphere. The communication links between Earth assets and lunar assets, such as the LOP-G and the LRS, could be analyzed with the same methodology.

4. Receiver Architecture

The block diagram of the K/Ka-band receiver (RX) is illustrated in Figure 3. The receiver exploits a dual conversion superheterodyne architecture [15,16]. The novelty of the proposed design is related to the adoption, for space applications, of commercial components originally developed for the military and for the automotive markets, i.e., for sectors where miniaturization and low cost are traditionally associated to high reliability levels. The receiver front-end operates a first down-conversion to an IF of 3.7 GHz. It consists of a two stages low noise amplifier (LNA), an image rejection filter (F2), a sub-harmonically pumped (×2) mixer (M1), an IF filter (F3) and a first stage of IF amplification (A1). The half frequency LO is generated by a microwave phased locked loop (PLL) synthesizer, this ensures a low near-carrier phase noise as well as frequency stability and agile channel selection. In the system, a pair of notch filters (F5, F4) are used to get rid of the spurious synthesizer signals and of the mixer feed through. For the K-band the LO frequency varies from 9.425 to 9.725 GHz; for the Ka-band, instead, the LO is in the range between 11.900 to 13.150 GHz.

At the front-end input a ferrite isolator and a preselection bandpass filter (F1) ensure a good input matching and an out-of-band interference limitation (including that originated by the downlink transmitter) respectively. Since, in this position, the insertion losses are critical, rectangular waveguide components will be adopted (WR34 for the K-band and WR28 for the Ka-band). For the same reason the image reject filter (F2) is placed after two LNA stages. In this way it is possible to: (i) minimize the RX noise; (ii) reduce the impact of the image filter attenuation on the overall noise figure. The second point is very important, since low cost filter implementations can be adopted. Among several possibilities, the substrate integrated waveguide (SIW) technology was selected as the candidate for preliminary experiments. This is a planar approach that leads to self shielding, compact structures: in such a way the image filter can be directly integrated in the front-end printed circuit board (PCB), with advantages in terms of compactness and reliability.
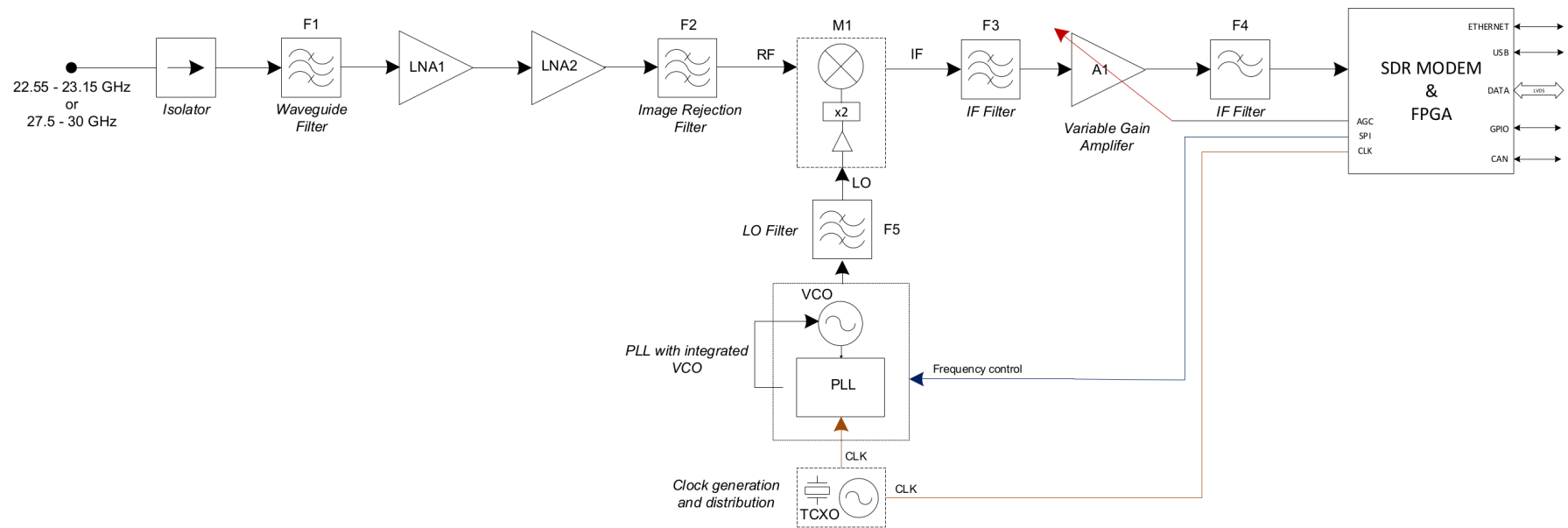
Figure 3. Block diagram. Simplified block diagram of the K/Ka band very-high data rate receiver. In the figure the Low-Noise Amplifier stages are indicated with LNA; F1 is the pre-selection filter; F2 is the image-rejection filter; M1 is the first mixer; VCO is the Voltage Controlled Oscillator that is stabilized by a Phase Locked Loop (PLL). The Reference signal is provided by a Temperature Compensated Crystal Oscillator (TCXO). Radio Frequency (RF) signal, Local Oscillator (LO) signal and Intermediate frequency (IF) signal identify the down-conversion mixer operation.

The second frequency conversion occurs within the software defined radio (SDR) connected after the front-end. Such a device, which is available as a system-on-chip (SoC), includes the quadrature demodulators and provides the I/Q samples to a digital modem, which, in turn, implements all the decoding and error correction functions of the selected protocol stack (DVB-S2). The modem is implemented as a custom solution via a state-of-the-art field programmable gate array (FPGA). Finally, it is worth noting that the SDR derives a receiver signal strength indicator (RSSI) signal that is acquired by the receiver central processing unit (CPU) and that is used to implement an automatic gain control (AGC) loop by adjusting the IF amplifier gain.

4.1. Linearity and Signal Levels

A preliminary system analysis can be obtained from the characteristics of the front-end building blocks, as they are reported in the corresponding data sheets. These characteristics are summarized in Table 4 and can be used to evaluate gain, noise and linearity of the receiver. The first row of the table quotes the short stage name used to identify each block in Figure 3.

The overall gain of the RX chain is estimated, under the hypothesis of conjugate impedance matching among the stages, as the product (sum in dB) of the individual gains. The gain of both image and IF filters have been assumed to be -3 and -4 dB respectively. These values are compatible with the planar technologies (substrate integrated waveguides and microstrip) that will be adopted for the realization of these filters [17]. The overall gain of the RX front-end is about 46 dB. In Table 4, no variable gain amplifier (VGA) stages are considered here (there is an AGC also within the SDR). As an option, the first IF stage could be replaced by a VGA, or followed by a controlled attenuator.

Table 4. Specification Breakdown of the Receiver Building Blocks.

Par.	Unit	I Isol.	F1 Pre. BPF	LNA 1 LNA Chain	LNA 2	F2 Img. BPF	M1 Mixer	F3 IF BPF	A1 IF Amp.	F4	SDR
G	(dB)	-0.4	-0.6	25	25	-3	-12	-4	17	-1	0–65
F	(dB)	0.4	0.6	2.0	2.0	3.0	12.0	4.0	3.0	1	3.8
P_{1dB}	(dBm)	–	–	-11	-11	–	3	–	1	–	n.a.
IIP_3	(dBm)	–	–	0	0	–	12	–	12	–	-17
Tech.		RWG	RWG	MMIC	MMIC	SIW	MMIC	MSTR	MMIC		IC

Note that, in Table, RWG stands for Rectangular WaveGuide; SIW stands for Substrate Integrated Waveguide; MSTR stands for MicroSTRip; IC stands for Integrated Circuit (silicon based) and MMIC stands for Microwave Monolithic Integrated Circuit (typically GaAs based).

The noise figure of the receiver, F_{RX}, is determined with the Friis' formula assuming a conjugate matching among the stages. The down-conversion chain is composed by F2, M1, F3, A1 and F4. Its noise figure is approximately equal to 22 dB, i.e., the sum in dB of the noise figures of F2, M1, F3 and A1 (this because F2, M1 and F3 are all passive devices). Using this value as an intermediate step, a total figure $F_{RX} = 3.01$ dB is estimated. By omitting F1, the noise figure can be as low as 2.4 dB and reduces to 2 dB if also the ferrite isolator is removed; this comes at the expense of a lower immunity of the receiver to out-of-band interferences and of a worse input matching.

The 1 dB compression point of the proposed receiver is limited by that of the mixer. Dividing the 1 dB compression point of M1 ($+3$ dBm at the input) by the gain of F1, LNA1, LNA2 and F2 (equal to 46 dB) one finds $P_{1dB} = -43$ dBm, which is the input-referred compression point of the receiver. Similarly, also the third-order intercept point is limited by the mixer. As a first approximation, dividing the IIP_3 of M1 ($+12$ dBm) by the gain of F1, LNA1, LNA2 and F2 (46 dB), one obtains $IIP_3 \approx -34$ dBm. More accurate calculations, accounting for the intermodulation distortions of LNA1 and LNA2, gives an $IIP_3 \approx -34.4$ dBm.

The receiver Spurious Free Dynamic Range ($SFDR$) is given by:

$$SFDR = \frac{2}{3}\left(IIP_3 + N_i\right) \tag{7}$$

where all the quantities are expressed in dB and dBm. For a 50 MHz IF bandwidth (i.e., for the previously evaluated noise floor N_i) one gets $SFDR \approx -39.7$ dB. This means that, until the in-band interference level is below -54.3 dBm (at the input), the third order intermodulation will remain below the noise floor, having no measurable effects.

Figure 4 reports a comprehensive view of the levels involved in both the uplink and in the receiver front-end. In particular the left axis represents the EIRP of ground transmitters on Earth whereas, the right axis, is the power level at the receiver input, on the Moon. The two vertical axes are scaled by -191 dB, a quantity equal to the receiver antenna gain (about $+40$ dBi) summed with the path loss for zenith and clear sky conditions (about -231 dB) in the K-band. The nomogram represents also the receiver noise floor and the linearity limits related to the 1 dB compression point and to the third-order intermodulation (i.e., to the $SFDR$). The nominal $+115$ dBm EIRP of the ground station sets the received power to about -76 dBm, 18 dB above the noise floor. As already discussed, however, such a margin is optimistic and serves to guarantee for non zenithal links and atmospheric attenuation.
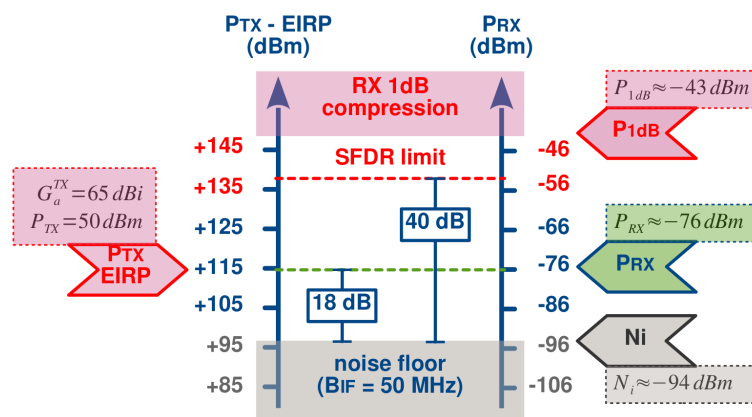
Figure 4. Signal levels. Comparison between transmitted effective isotropic radiated power (EIRP) of the ground station and received power levels at 22.85 GHz. For a link distance of 384.4×10^3 km the path loss is -231 dB, corresponding to Zenith and clear sky conditions. The RX axis also reports the noise floor (for 50 MHz IF bandwidth), the 1 dB compression point and the $SFDR$ limit.

4.2. Phase Noise Impairments

One of the main impairments in low-cost receivers is due to the phase-noise of the adopted PLL synthesizers. Although an accurate modeling of the phase noise is commonly available in modern electronic computer aided design (CAD) tools, it is not present in STK [9], the multi-physics software used for both the orbits and the link budget computations. In order to deal with this problem, a co-simulation between a CAD tool like Advanced Design System (ADS) and STK can be performed [18]. This paper uses a novel approach that, although approximated, is very light, easily integrable within STK and accurate at the same time.

As shown in ([19], p. 447), the Error Vector Magnitude (EVM) of modulated signals in the presence of phase-noise can be evaluated according to:

$$\text{EVM}_{rms} \simeq \sqrt{\frac{1}{\text{SNR}} + \Phi_{rms}^2} \qquad (8)$$

where SNR is the signal to noise ratio due to the additive (thermal) noise. This relation, which is an approximation for small phase errors Φ, has a very important consequence: in receivers, the EVM degradation due to phase-noise is similar to that produced by an equivalent increase of the SNR. As a result, an effective signal to noise ratio SNR_{eff} can be introduced as a cumulative parameter accounting for both the thermal noise and the oscillator phase-noise:

$$\frac{1}{\text{SNR}_{eff}} = \frac{1}{\text{SNR}} + \Phi_{rms}^2 \tag{9}$$

Equation (9) means that, in receivers, the phase-noise sets the upper SNR limit: indeed one has $\text{SNR}_{eff} \leq 1/\Phi_{rms}^2$. From the above theory it is apparent that the phase error Φ_{rms}^2 has to be determined. This can be done quite simply as shown in ([20], p. 8) by integrating the phase-noise spectrum $S_\phi(f)$:

$$\Phi_{rms}^2 = n^2 \int_{f_{min}}^{f_{max}} S_\phi(f)\, df \tag{10}$$

where n is the multiplication factor of a frequency multiplier (if present), and the integration frequency range is limited by f_{min} and f_{max}. The importance of (9) is that it establishes an equivalence between the phase error and the SNR. In particular, it shows that it is possible to determine an equivalent level of input additive noise which causes the same rms angular error of the given phase-noise in the I/Q scatter plot. On this basis it is possible to define an effective receiver noise figure that accounts for the local oscillator phase-noise too. At the receiver output the signal to noise ratio obeys to (9):

$$\frac{1}{\text{SNR}_{eff}} \simeq \frac{N_o}{S_o} + \Phi_{rms}^2 \tag{11}$$

being S_o and N_o the output signal and noise power respectively. Equivalently we can assume an ideal receiver (with no thermal noise and no phase-noise) and refer all the quantities to the input:

$$\frac{1}{\text{SNR}_{eff}} \simeq \frac{N_i + S_i\,\Phi_{rms}^2}{S_i} \tag{12}$$

where S_i and N_i are the input signal and noise power levels. The numerator of such an expression can be seen as an effective input noise power N_i^{eff} accounting for the phase-noise:

$$N_i^{eff} \simeq N_i + S_i\,\Phi_{rms}^2 \tag{13}$$

Now, expressing N_i^{eff} in terms of an effective noise figure F_{RX}^{eff} and N_i in terms of the conventional noise figure F_{RX} one gets:

$$k_B\, F_{RX}^{eff}\, T_0\, B_{IF} = k_B\, F_{RX}\, T_0\, B_{IF} + S_i\,\Phi_{rms}^2 \tag{14}$$

Finally, assuming $S_i = P_{RX}$ (true for constant envelope signals like QPSK), the above relationship can be used to derive the effective noise figure F_{RX}^{eff} in terms of the other system parameters:

$$F_{RX}^{eff} = F_{RX} + \frac{P_{RX}}{k_B\, T_0\, B_{IF}}\,\Phi_{rms}^2 \tag{15}$$

This equation states a very interesting fact: In order to account for the local oscillator phase-noise, the receiver noise figure is increased by a quantity proportional to the squared phase error multiplied by the input power referred to the noise power in the receiver bandwidth. As a result, there are two asymptotic cases: Low quality signals and high quality signals. In the first case the effective signal to noise ratio is limited by the receiver noise figure whereas, in the second case, it is limited by the local oscillator phase-noise. From (15) follows that the effective SNR in (9) can be evaluated, considering the antenna noise temperature T_a, as for the conventional noise figure:

$$\text{SNR}_{eff} \simeq \frac{P_{RX}}{k_B\left[T_a + \left(F_{RX}^{eff} - 1\right) T_0\right] B_{IF}} \tag{16}$$

To apply the above theory we consider, as first local oscillator, the ADF5356 microwave frequency synthesizer (Note that only the phase noise of the first local oscillator is considered. This because the second conversion happens inside the SDR, whose local oscillator has a much better phase noise than the ADF5356). Its phase-noise is shown in Figure 5 for a 13.6 GHz carrier (output B of the device) with a loop filter having a 2 kHz bandwidth. The reference frequency to the phase-frequency detector (PFD) is 61.44 MHz. The black line with diamonds represents the measurements reported in the device data-sheet ([21], p. 13). According to ([20], p. 41), the closed-loop synthesizer phase-noise can be modeled as:

$$S_\phi(f) = \begin{cases} \beta & \text{if } f < f_L \\ \dfrac{\beta}{(f/f_L)^3} & \text{if } f_L \le f < f_C \\ \dfrac{\beta}{(f_C/f_L)^3 (f/f_C)^2} & \text{if } f \ge f_C \end{cases} \tag{17}$$

with the following model parameters: $\beta = 1.25 \times 10^{-7}$ s, $f_L = 6$ kHz and $f_C = 100$ kHz. The fitting between measurements and model is also illustrated in Figure 5 (purple line).
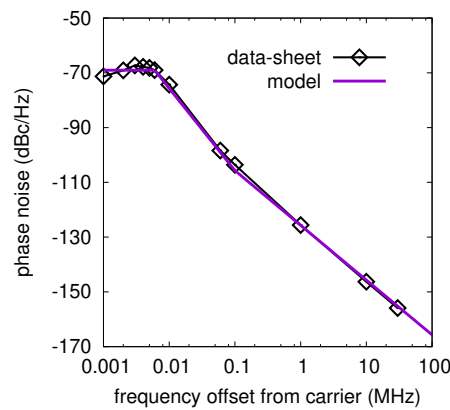
Figure 5. ADF5356 phase-noise: data-sheet vs model. The output frequency is 13.6 GHz (output B), the reference frequency to the phase-frequency detector (PFD) is 61.44 MHz and the loop filter has a 2 kHz bandwidth. The model parameters are: $\beta = 1.25 \times 10^{-7}$ s, $f_L = 6$ kHz and $f_C = 100$ kHz.

The phase-noise model reported in (17) can now be exploited to compute the integral in (10) and, thus, the phase error. Assuming $f_{min} \ge f_L$ and $f_{max} \ge f_c$ one gets:

$$\Phi_{rms}^2 = \frac{n^2 \beta f_L}{2} \left[\left(\frac{f_L}{f_{min}} \right)^2 + \left(\frac{f_L}{f_C} \right)^2 - 2 \frac{f_L^2}{f_C f_{max}} \right] \tag{18}$$

On the other hand, for $f_{min} < f_L$ and $f_{max} \ge f_c$ one obtains:

$$\Phi_{rms}^2 = n^2 \beta (f_L - f_{min}) + \frac{n^2 \beta f_L}{2} \left[1 + \left(\frac{f_L}{f_C} \right)^2 - 2 \frac{f_L^2}{f_C f_{max}} \right] \tag{19}$$

To deal with a numerical case, a QPSK signal is considered with 16200-bits DVB-S2 short frames, i.e., with $M_s = 8100$ symbols per frame (the QPSK implies 2 bits per symbol). The minimum frequency is assumed equal to the frame frequency: $f_{min} = f_s / M_s$, where f_s is the symbol rate. For the computations it is assumed $n = 2$ since, in the developed receiver, a sub-harmonic mixer (with an internal frequency doubler) is adopted. The phase errors are evaluated, for three symbol rates, using the above expressions and the results are quoted in Table 5. From this table is apparent that a 3.8° rms phase error is obtained for a 500 ksym/s signal, whereas the same error reduces to 2.2° at 50 Msym/s.

Table 5. Phase Errors versus the Symbol Rate.

Symbol Rate (Msym/s)	f_{min} (Hz)	f_{max} (MHz)	Φ_{rms}^2 (rad^2)	Φ_{rms} (degrees)
0.5	62	0.5	4.47×10^{-3}	3.8
5	617	5	4.20×10^{-3}	3.7
50	6173	50	1.42×10^{-3}	2.2

The final step is the estimation of the effective noise figure F_{RX}^{eff} and the comparison between C/N and SNR$_{eff}$. These computations are illustrated in Table 6 for a received power of -76.5 dBm (i.e., the maximum level for a zenith link) and of -91 dBm (i.e., 3 dB above the receiver noise floor for $B_{IF} = 50$ MHz). An antenna noise temperature $T_a \approx T_0 = 290$ K is assumed. From the analysis of the table emerges that the ADF5356 frequency synthesizer is adequate for this kind of radio receiver and that its phase-noise is a limiting factor only for high quality signals, i.e., for low data rate (narrow IF bandwidths) and high received power levels.

Table 6. Effective Noise Figure F_{Rx}^{eff}, C/N and SNR$_{eff}$ versus the Symbol Rate.

Symbol Rate (Msym/s)	Φ_{rms}^2 (rad^2)	P_{RX} (dBm)	$k_B\,T_0\,B_{IF}$ (dBm)	F_{RX} (dB)	F_{RX}^{eff} (dB)	C/N (dB)	SNR$_{eff}$ (dB)
0.5	4.47×10^{-3}		-117		17.2	37.5	23.3
5	4.20×10^{-3}	-76.5	-107	3	8.3	27.5	22.2
50	1.42×10^{-3}		-97		4.5	17.5	16.0
0.5	4.47×10^{-3}		-117		4.6	23.0	21.4
5	4.20×10^{-3}	-91.0	-107	3	3.2	13.0	12.8
50	1.42×10^{-3}		-97		3.0	3.0	3.0

4.3. New Receiver Features

From a digital point of view, the receiver will be equipped with new features, namely: Autonomous Doppler shift compensation, autonomous determination of the uplink signal characteristics and autonomous handover between base stations.

A first estimation of the Doppler shift is reported in Table 3. From the analysis of these data it is clear that any new functionality of the lunar receiver should consider the presence of a Doppler shift and of the associated Doppler compensation methods. Recently investigated techniques in the field of Doppler correction adopt a combination of search-range techniques and fast Fourier transform (FFT) [22,23]. These techniques, based on open-loop architectures and maximum likelihood estimation, can increase the acquisition probability and reduce the carrier frequency estimation error. A possible solution makes use of Doppler estimation and compensation techniques originally developed for high-mobility digital video broadcasting terrestrial receivers based on multi-carrier techniques [24]. These techniques can be adapted to a single-carrier satellite scenario by inserting a specially designed preamble that facilitates the estimation of the Doppler shift. Special preambles have been exploited, for instance, also in the DVB-S2 standard [25]. This Doppler compensation technique allows the receiver to acquire the signal lock even in the presence of extreme values of frequency shifts.

The lunar receiver should be able to detect the presence of a first signal, for instance of an E-LS link, and of a second signal, for instance due to an LO-LS link. In some cases, one of the two signals could be an unwanted interference to be suppressed. Therefore, it is important that the lunar receiver is able to distinguish two signals transmitted at the same time and to determine the characteristics (such as, for instance, central frequency, SNR, Doppler shift, symbol rate, modulation, code rate) of both signals. The determination of the presence or absence of a signal is a spectrum sensing problem that is also the first task of a cognitive radio network. In this case the proposed solution can be obtained by a combination among energy detection strategy (used to evaluate the power of the two signals), FFT and correlation techniques (to determine modulation and rate parameters).

Finally, in order to maintain an E-LS communication link, handover is required. In this way, the lunar receiver can be served by the best-located Earth transmitting station. In satellite networks, several categories of handover do exist. In the present lunar scenario, the lunar receiver does not transmit the received signal quality to the Earth stations. Therefore, the lunar receiver can neither initiate nor control the handover. Consequently, the lunar receiver should be able to autonomously detect when the Earth stations perform the handover [26]. Here the key idea is to allow the lunar receiver to detect two or more signals, and to successively select or combine the signals themselves. Two solutions are possible. In both solutions, the Earth stations initiate the handover by allowing, during the handover, the simultaneous transmission of the same signal from two different Earth stations. In the first solution, called a hard handover, the lunar receiver detects the two signals separately and then selects the most powerful one based on a link quality criterion. In the second solution, called soft handover, the lunar receiver jointly detects the two received signals, combining them after Doppler estimation and correction. Such a solution may require a specially designed preamble (like the one of DVB-S2) or a cyclic prefix and additional processing at the lunar receiver to constructively combine the two signals without link loss.

4.4. Radiation Dose and Countermeasures

Concerning ionizing radiation, cislunar environment is quite challenging, therefore, with respect to radiation tolerance, the following methodology will be adopted:

- The receiver PCB will be shielded by an Aluminum case of adequate thickness;
- Thanks to the miniaturization, allowed by extensive usage of ICs, a circuit redundancy can be effectively applied to the whole receiver or to a part of it (the K/Ka-band front-end, for example);
- High reliability components (automotive grade, military grade, radiation hardened and space grade) can be provided by the chip makers, if strictly needed by the considered application.

The lunar radiation environment, indeed, is characterized by its position, which is located beyond the Earth's protective atmosphere and magnetosphere. The overall computation of the absorbed total ionizing dose should consider the dominant contribution due to the crossing of Van Allen Belts during the path from Earth towards Moon. Beyond Van Allen Belts, in transit and on the lunar surface, the main sources of ionizing radiation are galactic cosmic rays (GCR) and solar particle events (SPE). Since the latter source is widely variable according to solar behavior, Moon surface radiation cannot be determined once and for all.

Approximately, given that radiation tolerance for components off the shelf (COTS) starts from 5 krad upwards, an adequate aluminum shielding is in the range of few millimeters for a lifespan of several months. To this purpose one could also exploits the experience gained in the past about radiation shielding in manned missions, since this is the only strategy that can be used to protect human beings from ionizing radiation effects.

5. Results

In order to verify the proposed concept, a receiver breadboard was realized exploiting COTS and evaluation boards (EVBs) as illustrated in Figure 6. The receiver prototype is based on two subsystems: i) the Ka-band front-end assembly, ii) the SDR and FPGA-based modem assembly. The Silicon Infusion Zaltys DVB-S2 modulator and demodulator IP cores realize the digital baseband section of the high performance DVB-S2 compliant modem. The cores are implemented directly in hardware and require minimal software interaction. The modem receive engine delivers excellent demodulation performance and includes LDPC, Bose-Chaudhuri-Hocquenghem (BHC) codes for soft decision and forward error correction (FEC) decoding to fully recover the transmitted Baseband Frames (BBFRAMES). Futhermore, the DVB-S2 standard includes a frame header that can be used to estimate carrier offset due to a Doppler shift. The Zaltys DVB-S2 Demodulator supports automatic handling of carrier offsets during acquisition of up to $\pm 10\%$ of the symbol rate.

Two frequency bands are considered in the present study, namely the K-band from 22.55 to 23.15 GHz and the Ka-band from 27.5 to 30 GHz. The front-end breadboard operates in the Ka-band with the purpose to determine the system performance in the most critical case, i.e., at high frequencies. The first IF signal (3.7 GHz) is obtained by means of a sub-harmonically pumped mixer, although fundamental mixers could, in principle, be used [27]. Indeed a sub-harmonically ($\times 2$) mixer requires an half-frequency LO in the range between 11.90 to 13.15 GHz and, such a signal, is easily generated by a PLL synthesizer.

The front-end prototype uses a commercial image reject filter implemented in rectangular waveguide, featuring a 28.65 GHz center frequency with a 300 MHz bandwidth. Such an approach, however, cannot be adopted neither in the engineering model, nor in the flight model since it is too bulky and expensive. The technology selected for the final application is based on SIW approach. With this method, a waveguide-like filter can be realized in the very same receiver PCB; the cavities being defined by the top and bottom metal layers and, laterally, by a series of carefully designed via-holes. With respect to microstrip or coplanar-waveguide (CPW) filters, the SIW technology allows for high Q-factor cavities and do not require any additional shielding, i.e., it leads to self shielding circuits.


(**a**) Ka-band front-end   (**b**) SDR and modem
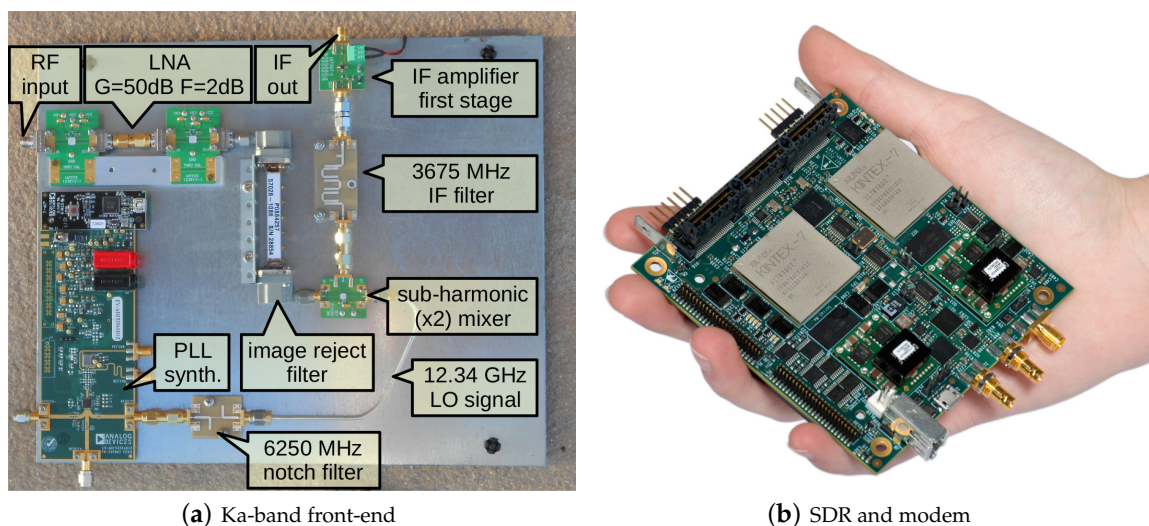
Figure 6. Prototypes. (**a**) Ka-band front-end breadboard operating from 27.5 to 30 GHz, (**b**) SDR and custom FPGA define both-based modem board. The 3.7 GHz IF signal is obtained by a sub-harmonically pumped mixer. The half-frequency LO is in the range between 11.90 to 13.15 GHz and it is generated by a PLL synthesizer.
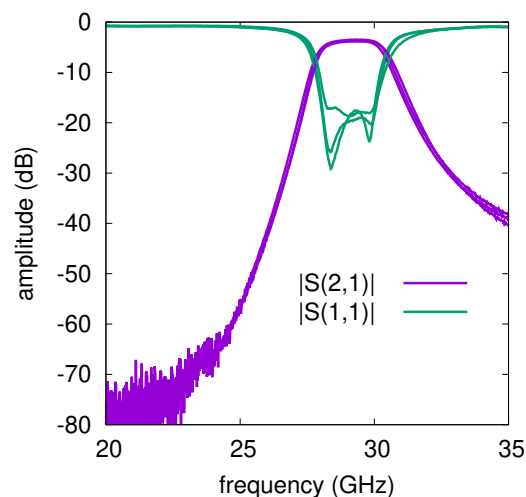
An image reject SIW filter is implemented in a low cost RO4350 material (thickness $h = 0.25$ mm, relative permittivity $\epsilon_R = 3.48$, loss factor $\tan \delta = 0.004$) as a proof-of-concept. The filter is designed according to the methodology proposed in [28] and is centered at 29.1 GHz. Figure 7a shows the fabricated circuit prototype: it uses four iris-coupled cavities and it is fed by two 50 Ω grounded CPW transmission lines. The PCB is 28 mm long and two coaxial-to-CPW launchers are used for measurement purposes. The measured frequency response of the filter is illustrated in Figure 7b: The filter insertion loss is of about 3.6 dB, including the feeding lines and the two launchers, whereas the return loss is around -20 dB at center frequency. The half-power bandwidth is equal to 2.5 GHz. In order to verify the repeatability of the fabrication process, three different circuits from the same lot have been tested: The frequency responses are very close (i.e., $|S(2,1)|$ within ± 0.2 dB in the pass band), as testified by Figure 7b. It is worth to note here that, in order to speed-up the SIW filter design, an automatic layout generation similar to that reported in [29] could be adopted, along with full-wave electromagnetixc solvers [30,31].

The measurement of the receiver front-end noise floor is reported in Figure 8a. In this case the RF input is terminated on a matched load at ambient temperature. The spectral noise density at the 3.7 GHz

IF output is about -128.9 dBm/Hz (see marker) and is clearly shaped by the 300 MHz bandwidth of the image reject filter (i.e., the rectangular waveguide filter mounted on the breadboard prototype). The IF spectrum of Figure 8b, instead, corresponds to a -60 dBm, 28.65 GHz CW signal at the input. The delivered IF power is -19.6 dBm (see marker), thus resulting in a transducer power gain of 40.4 dB. As a consequence, the input spectral noise density can be estimated as: $-128.9 - 40.4 = -169.3$ dBm/Hz which, for a 50 MHz signal bandwidth, gives a receiver noise floor of about -96 dBm, in agreement with the previous system analysis.
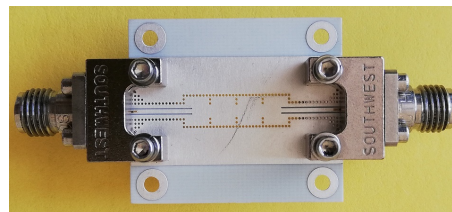
(**a**) fabricated circuit

(**b**) experiment

Figure 7. Image filter. 29.1 GHz image reject filter implemented in substrate integrated waveguide (SIW) technology: (**a**) layout; (**b**) experiment. The filter is realized on RO4350 material with $h = 0.25$ mm, $\epsilon_R = 3.48$ and $\tan \delta = 0.004$. The measured insertion loss is of about 3.6 dB including the feeding lines and the two coaxial-to-coplanar waveguide (CPW) end launchers. The return loss is around -20 dB at center frequency. The three measured prototypes show very close frequency responses, testifying the reproducibility of the fabrication process.

A more accurate characterization of the receiver noise performance requires the measurement of its noise figure. This was done exploiting the Y-factor method, as described in [32,33]. The N9918A Field-Fox from Keysight (in spectrum analyzer mode) was used to measure the delivered noise power at the 3.7 GHz IF output. In order to reduce the systematic errors due to the spectrum analyzer noise figure, a 15 dB preamplifier was adopted, setting to $F_{SA} \approx 22$ dB the overall noise figure of the measurement system. This value was used in the correction of the measured data according to ([32], p. 14). The measurements were carried out with the Y-factor method using a 40 GHz, FSW series, Rodhe & Schwarz spectrum analyzer (equipped with internal pramplifier and noise figure option). The 346C-K01 noise source from Agilent was adopted for the calibration: Its excess noise ratio is $ENR = 11.73$ dB at 28 GHz, whereas the input reflection coefficient is less than -16 dB in the on condition. The measurements are reported in Figure 8c,d for the available power gain and the noise figure versus frequency respectively. The receiver front-end overall noise figure is 3.4 dB whereas the corresponding gain is 40 dB. These values include the coaxial-to-CPW end launcher and the feeding

line insertion losses. With a separate set of measurements (carried out with a vector network analyzer), these have been evaluated at about 1.5 dB. As a result, de-embedding these losses from the receiver noise figure, a final value of about $F_{RX} \approx 3.4 - 1.5 = 1.9$ dB is obtained. It is worth noting here that the 2 dB ripple in the gain response is due to the mismatch between the two LNA stages and the transmission line length between them.


(**a**) IF with no input

(**b**) IF with 28.65 GHz input

(**c**) gain
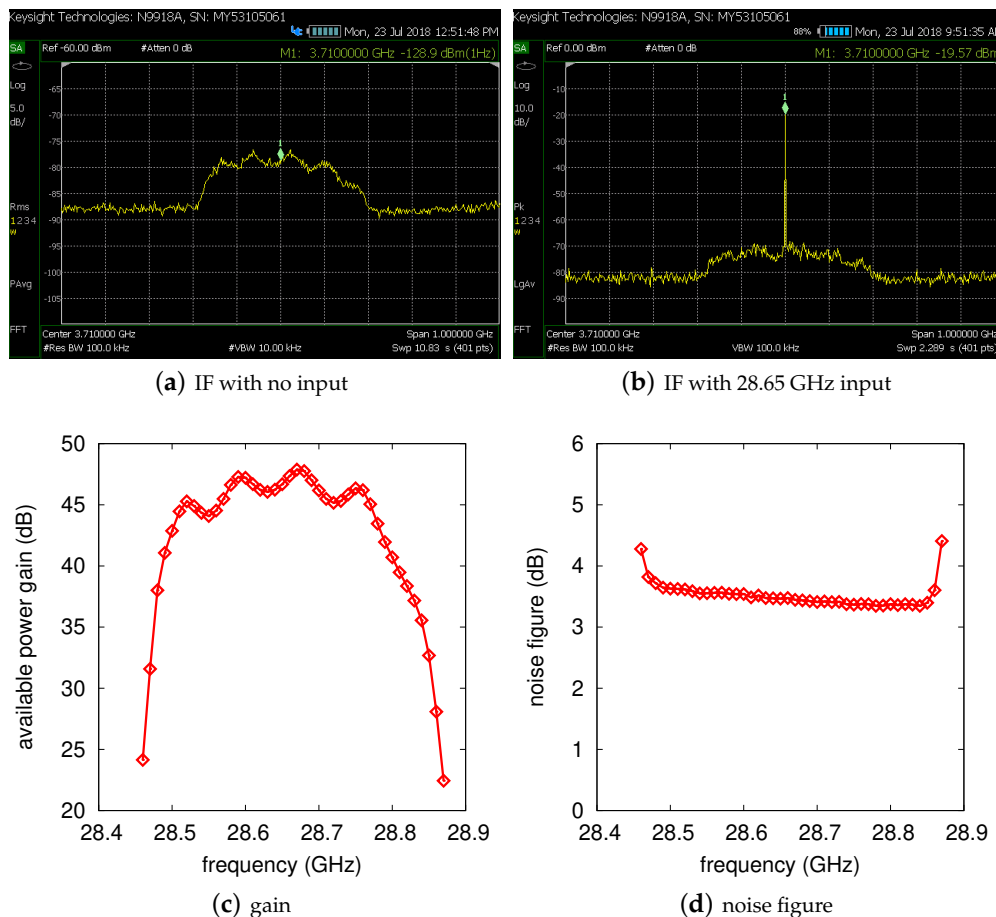
(**d**) noise figure

Figure 8. Gain and noise. Measured receiver breadboard performance in different conditions. (**a**) IF signal when the receiver input is terminated on a 50 Ω resistor at 295 K; (**b**) IF signal with a 28.65 GHz input signal having a −60 dBm available power; (**c**) gain versus frequency; (**d**) noise figure versus frequency. The receiver front-end overall gain is of about 46 dB and the corresponding noise figure is 3.4 dB. These values include the coaxial-to-CPW end launcher and the feeding line (insertion loss of about 1.5 dB). The gain and noise figure measurements have been carried out with the Y-factor method, exploiting the 346C-K01 noise source from Keysight ($ENR = 11.73$ dB at 28 GHz). The receiver breadboard uses a rectangular waveguide image reject filter with 300 MHz bandwidth.

The large signal gain of the receiver is depicted in Figure 9 as a function of the available input power at 28.65 GHz. For an input power of −100 dBm the gain is 46 dB, in agreement with that illustrated in Figure 8d. The input-referred 1 dB compression point is $P_{1dB} = -37$ dBm, which is suitable for the target moon receiver.

As a final test, the constellation in the I/Q plane at the output of the receiver breadboard (Ka-band front-end, SDR and demodulator) is measured for a QPSK signal at 40 Msym/s (see Figure 10). The modulated signal is centered at 28.6495 GHz, has a roll-off factor of 0.25 and a bandwidth of 50 MHz. The IF bandwidth of the SDR is set to 56 MHz, 77.5 dB above 1 Hz, the maximum allowed value; this also corresponds to the highest noise-floor level (worst case). The constellation is recorded for input signal power levels in the range from −50 to −80 dBm. Since the breadboard noise figure is 3.9 dB, the

−80 dBm case corresponds to a SNR of about 12 dB. This justifies the spreading observed in the I/Q plane. When the input power is increased such a spreading is reduced but not completely eliminated. Such a behavior is due to the phase noise of the local oscillators used in the down-converters, mainly that in the Ka-band front-end. In all cases of Figure 10 the receiver was in lock condition.
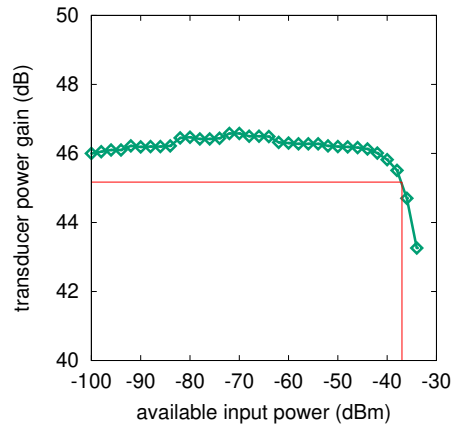

Figure 9. Linearity. Measured large signal receiver gain versus the available input power at 28.65 GHz. The input-referred 1 dB compression point is $P_{1dB} = -37$ dBm. This value includes the 1.5 dB insertion loss due to the coaxial-to-CPW end launcher and input feeding line.


(**a**) −60 dBm
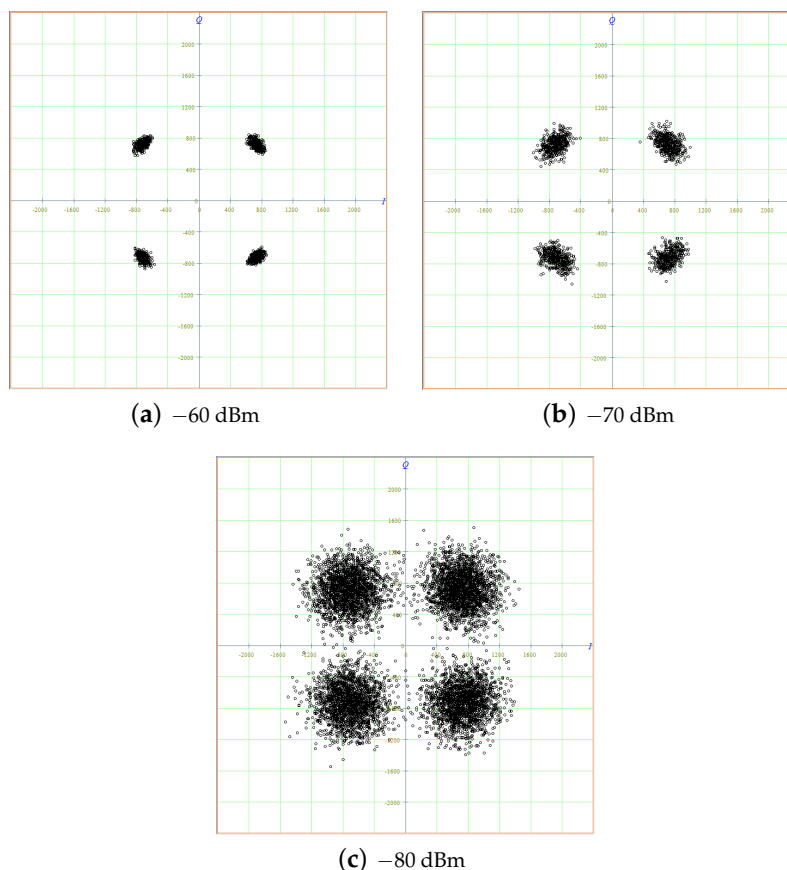
(**b**) −70 dBm

(**c**) −80 dBm

Figure 10. Quadrature phase shift keying (QPSK) test. Measured constellation in the I/Q plane for the whole receiver (Ka-band front-end, SDR and demodulator) at different input power levels. (**a**) $P_{RX} = -60$ dBm; (**b**) $P_{RX} = -70$ dBm; (**c**) $P_{RX} = -80$ dBm. A QPSK signal at 40 Msym/s, roll-off factor 0.25, is provided at the input. The receiver bandwidth is set to 56 MHz. Considering the breadboard noise figure, a 12 dB SNR is achieved in the −80 dBm case.

To test the receiver robustness, an interferer at 28.6505 GHz (i.e., at 1 MHz offset from the main signal center frequency) is injected at the receiver input. The interferer is a pure carrier and has the same -60 dBm power as the signal (the signal to interferer power ratio is $S/I = 0$ dB). The resulting power spectrum and I/Q constellation are represented in Figure 11. As a consequence of the interference, a rotation of the received data around the expected $(\pm\sqrt{2}, \pm\sqrt{2})$ points in the I/Q plane is observed. The receiver was in lock condition even in this case.
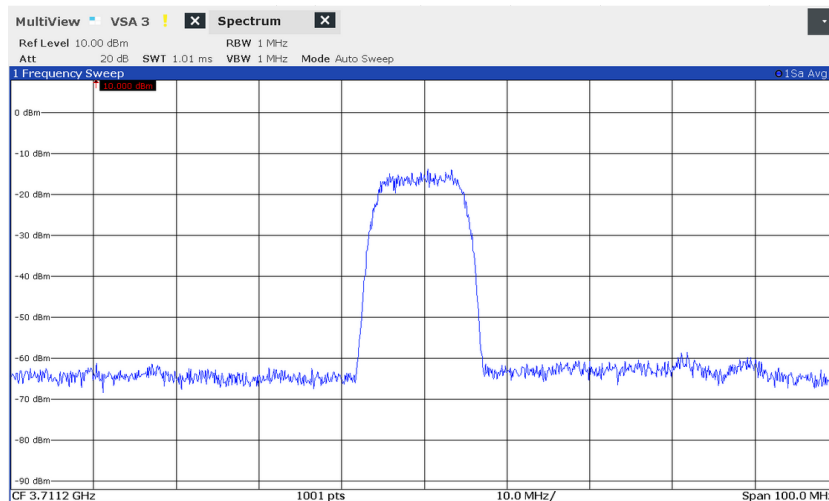
(**a**) spectrum
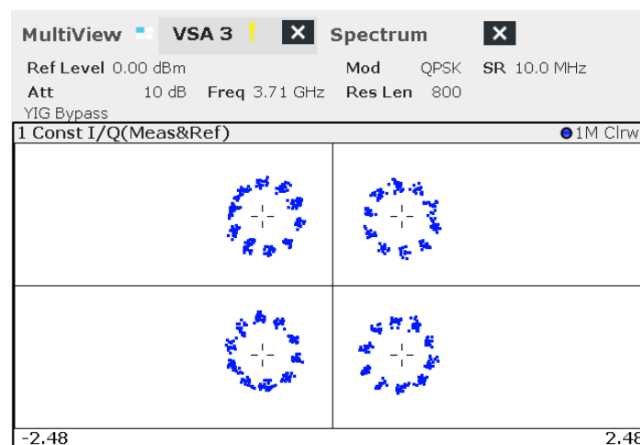
(**b**) constellation

Figure 11. In-band interference. Measured spectrum (**a**) and constellation in the I/Q plane (**b**) at the output of the receiver breadboard (Ka-band front-end, SDR and demodulator) for a QPSK signal at 40 Msym/s. The modulated signal has an available power of -60 dBm and is centered at 28.6495 GHz. An interferer is added at the receiver input. The interferer is a -60 dBm carrier at 28.6505 GHz (i.e., at 1-MHz offset). This justifies the rotation of the received data around the expected $(\pm\sqrt{2}, \pm\sqrt{2})$ points in the I/Q plane.

6. Discussion

An analysis of the state of the art is proposed in Table 7. The developed receiver compares well with two famous designs, the first from Alenia Sapce [34] and the second from Harris [35]. The power consumption of the Ka-band front-end, including the PLL synthesizer, is of about 2.48 W (breadboard measurements). The SDR (second conversion, demodulation, analog to digital conversion (ADC) and high-speed digital interfaces) consumes about 2 W with 56 MHz of IF bandwidth. The FPGA board with modem (digital signal processing, detector) and the CPU (at 20% of full capacity) consumes

another 3 W. The power supply unit (with DC-DC converter and regulators) dissipates about 0.5 W. As a result the total power consumption is of about 8 W, if all is switched on (no power saving strategies). Such a requirement is compatible with the capability of presently available electrical power subsystems (EPS) and, specifically, with the energy generation capabilities of deployable solar panels for cubesat platforms. Recent papers, indeed, show that this kind of panels can supply between 20 and 50 W, when correctly oriented to the Sun [36–38].

Table 7. State-of-the-Art for K/Ka-Band Receivers for Space Applications.

Ref.	Mission Scenario	f_0 (GHz)	FE Gain (dB)	F_{RX} (dB)	P_{1dB} (dBm)	Data Rate (Mb/s)	DC Power (W)	Mass (kg)
[34]	GEO satellites	27.50–31.00	55	2.3	−42	n.a.	5 (+)	0.2 (+)
[35]	International Space Station	22.52–23.12	n.a.	2.3	n.a.	12.5	n.a.	19.2 (*)
this work	Moon & cislunar space	22.55–23.15 27.50–30.00	46	1.9 (†)	−37	100	8	0.6 (‡)

(+) only Ka-band receiver front-end; (*) includes a 40 W transmitter unit; (†) noise figure equal to 3.4 dB with end-launcher and input CPW line; (‡) estimated value.

Concerning size and mass, it has been estimated that the proposed front-end can easily be integrated in a single PCB having a size of 9×9 cm^2. Three other similar boards are needed for the (i) software-defined radio, (ii) for the modem and CPU and (iii) for the power supply unit. Estimating a thickness of 1 cm for each board, a total volume of $9 \times 9 \times 4 = 324$ cm^3 is obtained. This implies an overall mass of about 0.6 kg if an average specific mass of 1.95 g/cm^3 is assumed for all the electronics.

The achieved miniaturization level is already compatible with cubesat platforms and will be further improved exploiting the single-chip solution that the microelectronic industry is developing for the ground-based 5G telecommunication and imaging systems [39–42]. This mean that cubesats could be exploited in future Moon exploration missions, as happened ìn the fall 2018 with the Mars Cube One (MarCO) satellites.

7. Conclusions

In the next years, the cislunar space will be the target for a variety of projects, such as the Lunar Orbital Platform-Gateway and the Lunar Relay Satellites. This calls for new technologies to be developed and, among them, for the set-up of a suitable telecommunications infrastructure. Such infrastructure should have the capability of carrying out the simultaneous multi-band communications between Earth, the Moon, including visiting (rovers) and descent/ascent (landers, terminals) vehicles, and other elements in cislunar orbit. Since this kind of missions employs many information-intensive (high resolution, high coverage, high duty cycle) sensors, high speed data links will be required.

The above scenario is investigated in the present paper and, specifically, the feasibility study of a high data rate receiver operating in the K/Ka band is carried out. Starting from a careful mission and system analysis, the main specifications of such a receiver are outlined. Particularly relevant are some new features that need to be considered in this applications, such as: Autonomous Doppler shift compensation, autonomous determination of the uplink signal characteristics and autonomous handover between base stations.

The foreseen receiver uses a low noise down-converter from K/Ka-band to a first IF at 3.7 GHz, a software defined radio for the second frequency conversion and the I/Q demodulation (including ADCs) and a FPGA-based decoder and data interface. A preliminary front-end breadboard operating between 27.5 and 30 GHz has been implemented. The breadboard is based on COTS and commercial EVBs and features a 46 dB gain, a 3.4 dB noise figure and a −37 dBm input-referred 1 dB compression point. A final demodulation test, carried on a QPSK signal at 40 Msym/s, show the feasibility of the proposed receiver, even on the basis of the low cost, off the shelf integrated circuits.

While the receiver design may seem a conventional one, it is worth mentioning once again that the aim of this work is to assess and validate the receiver concept according to those aspects that are critical for the success of a space mission. Indeed it can be considered as remarkable the fact that a receiver design (which can be assumed common practice for consumer applications) is proven to withstand all the challenges of the space environment, as stated in the discussion. This demonstrates that new approaches can be as reliable as traditional ones, and also more cost effective.

Author Contributions: F.A., P.M., L.R., V.P., S.B., R.V.G., L.R., G.B., F.F., P.B. (UniPG) and F.P., M.F., A.C., E.D.F., F.D. and A.G. (PicoSaTs) conceived the study; F.B. and F.G. (GMSpazio) simulated the mission scenario; E.P. and G.G. proposed an antenna solution; F.A., P.M., (UniPG) and F.P., M.F., A.C., E.D.F., F.D. and A.G. (PicoSaTs) designed the breadboard, performed the experiments and analyzed the data; G.N. (Silicon Infusion) designed and developed the DVB-S2 modem; P.P. and F.C. (PoliTO and ESA-ESTEC) critically revised the architectural and the breadboard design; P.G. (Paolo Gervasoni) and P.G. (Paolo Glionna) (Analog Devices) provided the components and supported the breadboard design; F.A. (UniPG) and A.G. (UniTs, PicoSaTs) wrote the paper; A.G. (UniTs, PicoSaTs) was the principal investigator of this research.

Conflicts of Interest: The authors declare no conflict of interest.

References

1. Berrilli, F.; Bigazzi, A.; Roselli, L.; Sabatini, P.; Velli, M.; Alimenti, F.; Cavallini, F.; Greco, V.; Moretti, P.; Orsini, S.; et al. The ADAHELI Solar Mission: Investigating the Structure of the Sun's Lower Atmosphere. *Adv. Space Res.* **2010**, *45*, 1191–1202. [CrossRef]
2. European Space Agency (ESA). Very High Data Rate Receiver for the Earth-Space Link in the 22 GHz Frequency for Future Moon Exploration Missions; 2018.
3. *Achieving Science with CubeSats: Thinking Inside the Box*; The National Academies Press: Washington, DC, USA, 2016.
4. *Radio Regulations*; International Telecommunication Union (ITU): Geneva, Switzerland, 2016.
5. McSpadden, J.; Mankins, J. Space Solar Power Programs and Microwave Wireless Power Transmission Technology. *IEEE Microw. Mag.* **2002**, *3*, 46–57. [CrossRef]
6. Yao, J.; Hew, Y.; Mears, A.; Huang, H. Strain Gauge-Enable Wireless Vibration Sensor Remotely Powered by Light. *IEEE Sens. J.* **2015**, *15*, 5185–5192. [CrossRef]
7. Rahmat-Samii, Y.; Manohar, V.; Kovitz, J. For Satellites, Think Small, Dream Big: A Review of Recent Antenna Developments for CubeSats. *IEEE Antennas Propag. Mag.* **2017**, *59*, 22–30. [CrossRef]
8. Chahat, N. A Mighty Antenna from a Tiny CubeSat Grows. *IEEE Spectr.* **2018**, *55*, 32–37. [CrossRef]
9. *Engineering Tools System Tool Kit (STK)*; Analytical Graphics, Inc.: Exton, PA, USA, 2019.
10. Zuccarelli, J.; Martorelli, V.; D'Arcangelo, O.; Rosa, A.D.; Pagana, E.; Mandolesi, N.; Valenziano, L. Onset & offset configuration for Ka-band reflectarray antenna. In Proceedings of the 3rd European Conference on Antennas and Propagation, Berlin, Germany, 23–27 March 2009.
11. Buttazzoni, G.; Comisso, M.; Cuttin, A.; Fragiacomo, M.; Vescovo, R.; Gatti, R.V. Reconfigurable phased antenna array for extending cubesat operations to Ka-band: Design and feasibility. *Acta Astronaut.* **2017**, *137*, 114–121. [CrossRef]
12. Gatti, R.V.; Rossi, R. A dual circularly polarized slot-fed horn array antenna with linear polarization-tracking feature. *Int. J. RF Microw. Comput. Aided Eng.* **2018**, *28*, 1–11.
13. *ITU-R Recommendation P.838-2, Specific Attenuation Model for Rain for Use in Prediction Methods*; International Telecommunication Union (ITU): Geneva, Switzerland, 2005.
14. *ITU-R Recommendation P.676-9, Attenuation by Atmospheric Gases*; International Telecommunication Union (ITU): Geneva, Switzerland, 2012.

15. Cuttin, A.; Alimenti, F.; Coromina, F.; Fazio, E.D.; Dogo, F.; Fragiacomo, M.; Gervasoni, P.; Gotti, G.; Gregorio, A.; Mezzanotte, P.; et al. A Ka-band Transceiver for CubeSat Satellites: Feasibility Study and Prototype Development. In Proceedings of the 48th European Microwave Conference, Madrid, Spain, 23–27 September 2018.

16. Gregorio, A.; Alimenti, F. CubeSats for Future Science and Internet of Space: Challenges and Opportunities. In Proceedings of the IEEE International Conference on Electronics, Circuits and Systems (ICECS), Bordeaux, France, 9–12 December 2018.

17. Mariotti, C.; Alimenti, F.; Mezzanotte, P.; Dionigi, M.; Virili, M.; Giacomucci, S.; Roselli, L. Modeling and Characterization of Copper Tape Microstrips on Paper Substrate and Application to 24 GHz Branch-Line Couplers. In Proceedings of the 43rd European Microwave Conference, Nuremberg, Germany, 6–10 October 2013; pp. 794–797.

18. Keysight Technologies. Applying System Analysis to SATCOM Mission Requirements and Channel Impairments. 2017. Available online: https://www.keysight.com (accessed on 20 March 2019).

19. Georgiadis, A. Gain, Phase Imbalance, and Phase Noise Effects on Error Vector Magnitude. *IEEE Trans. Veh. Technol.* **2004**, *53*, 443–449. [CrossRef]

20. Lacaita, A.; Levantino, S.; Samori, C. *Integrated Frequency Synthesizers for Wireless Systems*; Cambridge University Press: Cambridge, UK, 2007.

21. Analog Devices. ADF5355 Data Sheet, Microwave Wideband Synthesizer with Integrated VCO. 2017. Available online: https://www.analog.com (accessed on 20 March 2019).

22. Linty, N.; Presti, L.L. Doppler Frequency Estimation in GNSS Receivers Based on Double FFT. *IEEE Trans. Veh. Technol.* **2016**, *65*, 509–524. [CrossRef]

23. Zhang, Z.; Cheng, W.; Zhang, H. Search-Range-Correction-Based Doppler Shift Acquisition for Space Communications. *IEEE Trans. Veh. Technol.* **2016**, *65*, 3271–3284. [CrossRef]

24. Poggioni, M.; Rugini, L.; Banelli, P. A Novel Simulation Model for Coded OFDM in Doppler Scenarios. *IEEE Trans. Veh. Technol.* **2008**, *57*, 2969–2980. [CrossRef]

25. *Digital Video Broadcasting (DVB); Second Generation Framing Structure, Channel Coding and Modulation Systems for Broadcasting, Interactive Services, News Gathering and Other Broadband Satellite Applications*; Part 1: DVB-S2, Doc. No. ETSI EN 302 307-1 V1.4.1; European Telecommunications Standards Institute (ETSI): Sophia-Antipolis, France, 2014.

26. Chowdhury, P.; Atiquzzaman, M.; Ivancic, W. Handover schemes in satellite networks: State-of-the-art and future research directions. *IEEE Commun. Surv. Tutor.* **2006**, *8*, 2–14. [CrossRef]

27. Alimenti, F.; Mezzanotte, P.; Giacomucci, S.; Dionigi, M.; Mariotti, C.; Virili, M.; Roselli, L. 24-GHz Single-Balanced Diode Mixer Exploiting Cellulose-Based Materials. *IEEE Microw. Wirel. Compon. Lett.* **2013**, *23*, 596–598. [CrossRef]

28. Chen, X.P.; Wu, K. Substrate Integrated Waveguide Cross-Coupled Filter With Negative Coupling Structure. *IEEE Trans. Microw. Theory Tech.* **2008**, *56*, 142–149. [CrossRef]

29. Aluigi, L.; Alimenti, F.; Pepe, D.; Roselli, L.; Zito, D. MIDAS: Automated Approach to Design Microwave Integrated Inductors and Transformers on Silicon. *Radioengineering* **2013**, *22*, 714–723.

30. Alimenti, F.; Mezzanotte, P.; Roselli, L.; Sorrentino, R. Efficient Analysis of Waveguide Components by FDTD Combined with Time Domain Modal Expansion. *IEEE Microw. Guid. Wave Lett.* **1995**, *5*, 351–353. [CrossRef]

31. Alimenti, F.; Mezzanotte, P.; Roselli, L.; Sorrentino, R. A Revised Formulation of Modal Absorbing and Matched Modal Source Boundary Conditions for the Efficient FDTD Analysis of Waveguide Structures. *IEEE Trans. Microw. Theory Tech.* **2000**, *48*, 50–59. [CrossRef]

32. Agilent Technologies. Fundamental of RF and Microwave Noise Figure Measurements. 2000. Available online: https://www.keysight.com (accessed on 20 March 2019)

33. Alimenti, F.; Tasselli, G.; Botteron, C.; Farine, P.; Enz, C. Avalanche Microwave Noise Sources in Commercial 90-nm CMOS Technology. *IEEE Trans. Microw. Theory Tech.* **2016**, *64*, 1409–1418. [CrossRef]

34. Comparini, M.; Feudale, M.; Linkowski, J.; Ranieri, P.; Suriani, A. Fully Integrated Ka/K Band Hermetic Receiver Module. In Proceedings of the 30th European Microwave Conference, Paris, France, 2–5 October 2000.

35. Downey, J.; Reinhart, R.; Kacpura, T. Pre-flight Testing and Performance of a Ka-band Software Defined Radio. In Proceedings of the 30th AIAA International Communications Satellite System Conference (ICSSC), Ottawa, ON, Canada, 24–27 September 2012; pp. 1–13.

36. Clark, C. Huge Power Demand...Itsy-Bitsy Satellite: Solving the CubeSat Power Paradox. In Proceedings of the 24th Annual AIAA/USU Conference on Small Satellites, Logan, UT, USA, 9–12 August 2010; pp. 1–8.

37. Senatore, P.; Klesh, A.; Zurbuchen, T.; McKague, D.; Cutle, J. Concept, Design, and Prototyping of XSAS: A High Power Extendable Solar Array for CubeSat Applications. In Proceedings of the 40th Aerospace Mechanisms Symposium, NASA Kennedy Space Center, Cocoa Beach, FL, USA, 12–14 May 2010; pp. 431–444.

38. Santoni, F.; Piergentili, F.; Donati, S.; Perelli, M.; Negri, A.; Marino, M. An Innovative Deployable Solar Panel System for Cubesats. *Acta Astronaut.* **2014**, *95*, 210–217. [CrossRef]

39. Padovan, F.; Tiebout, M.; Neviani, A.; Bevilacqua, A. A 15.5–39GHz BiCMOS VGA with Phase Shift Compensation for 5G Mobile Communication Transceivers. In Proceedings of the 42nd European Solid-State Circuits Conference (ESSCIRC), Lausanne, Switzerland, 12–15 September 2016.

40. Zielska, A.; Juenemann, R.; Schiessl, A.; Tiebout, M. A True Differential Characterization of a 80 GHz Low Power Wideband Receiver Chip for Microwave Imaging Application. In Proceedings of the 7th European Microwave Integrated Circuit Conference, Amsterdam, The Netherlands, 29–30 October 2012.

41. Alimenti, F.; Zito, D.; Boni, A.; Borgarino, M.; Fonte, A.; Carboni, A.; Leone, S.; Pifferi, M.; Roselli, L.; Neri, B.; et al. System-on-chip microwave radiometer for thermal remote sensing and its application to the forest fire detection. In Proceedings of the 15th IEEE International Conference on Electronics, Circuits and Systems (ICECS), St. Julien's, Malta, 31 August–3 September 2008; pp. 1265–1268.

42. Aluigi, L.; Pepe, D.; Alimenti, F.; Zito, D. K-Band SiGe System-on-Chip Radiometric Receiver for Remote Sensing of the Atmosphere. *IEEE Trans. Circuit Syst. I Regul. Pap.* **2017**, *64*, 3025–3035. [CrossRef]